remote sensing

MDPI

Article

Monitoring *Dendrolimus punctatus Walker* Infestations Using Sentinel-2: A Monthly Time-Series Approach

Fangxin Meng [1,2], Xianlin Qin [1,2,*], Yakui Shao [1,2], Xinyu Hu [1,2], Feng Jiang [1,2], Shuisheng Huang [1,2] and Linfeng Yu [1,2]

[1] Institute of Forest Resource Information Techniques, Chinese Academy of Forestry, Beijing 100091, China; mengfx0208@163.com (F.M.); shaoyakui@ifrit.ac.cn (Y.S.); hxyuinu@163.com (X.H.); camellia_0601@163.com (F.J.); huangss@ifrit.ac.cn (S.H.); yulinfeng@ifrit.ac.cn (L.Y.)

[2] Key Laboratory of Forestry Remote Sensing and Information System, National Forestry and Grassland Administration, Beijing 100091, China

* Correspondence: qxl@ifrit.ac.cn

Highlights

What are the main findings?

- A Sentinel-2-based monthly monitoring framework integrating a Weighted Composite Index (WCI), time-series features, and Random Forest models successfully classified *Dendrolimus punctatus Walker* infestation severity with accuracies exceeding 86.9% (Kappa: 0.825–0.858) across 2019–2024.
- Multi-year monitoring revealed recurring outbreak events during the study period (2019, 2021, and 2023). Infestation dynamics generally progressed from scattered mild damage to more concentrated and severe distributions, indicating structured spatiotemporal patterns rather than strictly periodic cycles.

What are the implications of the main findings?

- The WCI approach synthesizing IRECI, EVI, and NDVI with temporal dynamics provides an operational and transferable methodology for precision forest pest monitoring using freely available satellite data, substantially reducing dependence on costly field surveys.
- Understanding biennial cyclical patterns and spatial progression of *Dendrolimus punctatus Walker* infestation enables monitoring modeling and strategic planning for proactive forest protection and sustainable ecosystem management.

Abstract

Infestations of *Dendrolimus punctatus Walker* (*D. punctatus*) pose significant threats to forest ecosystem health, necessitating accurate and efficient monitoring for sustainable forest management. A monthly monitoring framework integrating spectral bands, vegetation indices, time-series features, meteorological variables, and topographic characteristics was developed. First, cloud-free Sentinel-2 composites were generated via median synthesis, and training samples were selected by integrating GF-1/2 data. Subsequently, a Weighted Composite Index (WCI) was constructed through logistic regression to quantitatively classify infestation severity levels. Meanwhile, time-series features extracted from vegetation indices were incorporated to characterize temporal damage dynamics. Finally, Random Forest (RF) models were then trained for monthly monitoring, achieving overall accuracies exceeding 86.9% with Kappa coefficients ranging from 0.825 to 0.858. The Inverted Red Edge Chlorophyll Index (IRECI), Enhanced Vegetation Index (EVI), and Normalized Difference Vegetation Index (NDVI) exhibited the highest sensitivity to *D. punctatus* damage and

Check for updates

Academic Editor: Michael Sprintsin

Received: 1 December 2025
Revised: 30 December 2025
Accepted: 2 January 2026
Published: 6 January 2026

Copyright: © 2026 by the authors. Licensee MDPI, Basel, Switzerland. This article is an open access article distributed under the terms and conditions of the Creative Commons Attribution (CC BY) license.

thus received the greatest weights in the WCI. Time-series features ranked second in importance after vegetation indices, substantially enhancing model performance. Monitoring results from 2019 to 2024 revealed that *D. punctatus* infestation in Qianshan City exhibited an occurrence pattern progressing from mild to severe and from scattered to aggregated distributions, with major outbreak periods in 2019, 2021, and 2023 reflecting characteristic cyclical dynamics. This study advances existing quantitative monitoring methodologies for *D. punctatus* and provides technical support and a scientific foundation for precision pest monitoring and forest health management.

Keywords: *dendrolimus punctatus walker*; pest monitoring; Sentinel-2; random forest; time-series analysis

1. Introduction

Forest ecosystems are essential for regulating climate, conserving water resources, and maintaining global ecological balance [1]. However, the combined impacts of climate change and biological stressors pose significant threats to forest health, with pest infestation emerging as a key driver of forest degradation [2,3]. Annually, forest pests and diseases result in the loss of millions of hectares of forest, disrupting ecosystem structure and function [4,5]. Climate warming and altered precipitation patterns have increased both the frequency and intensity of pest infestation [6–8]. In the coniferous forests of southern China, periodic infestations of *D. punctatus* are particularly notable [9,10]. As a defoliating pest, *D. punctatus* can lead to widespread tree mortality during infestation, causing extensive damage that severely impacts sustainable forest management [11]. Therefore, developing monitoring models for *D. punctatus* infestation is crucial for the accurate identification and quantitative assessment of such disasters.

Remote sensing technology serves as a crucial tool for large-scale monitoring of forest pests by capturing the spectral responses of vegetation to biological stress [12,13]. Pest infestation leads to reductions in chlorophyll content [14], leaf water content [15], and changes in canopy structure [16]. These alterations manifest spectrally as decreased near-infrared reflectance [17], shifts in red-edge position [18,19], and increased shortwave infrared absorption [20], among other characteristics.

Satellite data from Landsat and Sentinel-2 have been extensively used in forest health assessments. Landsat time-series data have demonstrated strong capabilities in detecting and monitoring forest disturbances over large spatial scales. For instance, Ye et al. [21] developed a stochastic continuous change detection method using dense Landsat time series to monitor forest disturbances across the conterminous United States, revealing clear spatiotemporal patterns of disturbance dynamics. More recently, Tang et al. [22] demonstrated that fusing Landsat observations with Sentinel-2 and Sentinel-1 data via a fusion algorithm enables consistent detection of forest disturbances across heterogeneous tropical landscapes, highlighting the value of multi-sensor integration for large-scale monitoring. The Sentinel-2, with its enhanced spectral resolution (including red-edge bands), has further advanced forest health monitoring capabilities. Recent studies using Sentinel-2 time series and vegetation indices have shown higher sensitivity to subtle canopy changes induced by insects than traditional broadband indices, particularly in the early infestation stages. Abdullah et al. [23] found that Sentinel-2 red-edge vegetation indices outperformed Landsat-8 indices in detecting the early "green-attack" stages of bark beetles. Similarly, Huo et al. [24] demonstrated that Sentinel-2 red-edge bands and water-related

indices significantly improve the detection of insect-induced disturbance signals in forest time-series analyses.

Furthermore, the integration of multi-temporal Sentinel-2 imagery with advanced analytical methods has improved the ability to discriminate pest-induced stress from natural phenological variations. Candotti et al. [25] integrated multi-year Sentinel-2 observations with machine learning techniques to achieve higher accuracy in detecting and classifying bark beetle damage across different forest types. Recent work by Reinosch et al. [26] has further validated the effectiveness of Sentinel-2-based forest disturbance detection systems across diverse environmental conditions at the national scale. Sentinel-2 data have shown significant advantages in time-series monitoring [27]. Specifically, with 13 multispectral bands and spatial resolutions ranging from 10 to 60 m [28], Sentinel-2 has further demonstrated significant advantages in forest pest monitoring. In particular, its red-edge bands are sensitive to chlorophyll dynamics [29], enabling the effective identification of vegetation stress signals and the characterization of pest dispersal patterns [30,31].

Remote sensing methods for monitoring forest pests have progressed from single-date analyses to multi-temporal and time-series analyses [32]. This evolution reflects a shift toward multi-source data fusion, time-series analysis, and intelligent modeling. By constructing time-series features of vegetation indices, researchers can characterize dynamic changes in vegetation health, thereby revealing patterns of pest infestation [33,34]. The identification of such infestation relies heavily on detecting anomalous changes in time-series data [35,36], including declines in vegetation greenness, abnormal shifts in phenological characteristics, and trends in red-edge spectral features. Previous studies have shown that time-series analysis methods can effectively differentiate between spectral variations associated with natural growth and those induced by stress, thus providing a theoretical foundation for dynamic forest disturbance monitoring [37,38].

Despite significant progress in remote sensing-based forest pest and disease monitoring, methods for classifying the severity of pests and diseases still lack a unified standard and a simple, widely applicable operational procedure. In many studies, the definition of forest pest severity relies primarily on empirical classifications or is artificially determined based on leaf fall rates and damage proportions obtained from field surveys, and lacks statistically rigorous systematic optimization. For example, Meddens et al. [39] compared single-date and multi-date Landsat classification methods for detecting bark beetle-induced tree mortality and found that most grid cells exhibit intermediate levels of mortality; however, the severity thresholds were not optimized based on data distribution characteristics. Similarly, Rahimzadeh-Bajgiran et al. [40] conducted a classification assessment of spruce budworm infestation by integrating NDVI, EVI, and NDMI. The results showed that multi-index fusion can effectively distinguish between healthy stands and severely damaged stands, but the classification accuracy for light and moderate damage levels decreased significantly, reflecting the challenge of accurately separating continuous damage gradients. In the field of time-series remote sensing research, Jamali et al. [41] achieved early identification of bark beetle infestation based on Sentinel-2 time-series data and change detection methods, yielding good monitoring results. However, their severity thresholds mainly relied on preset change detection parameters rather than data-driven statistical optimization for different damage levels. Relevant review studies indicate that although multi-source remote sensing and multi-index methods show great potential for pest and disease identification, inconsistent threshold setting continues to limit the repeatability of severity grading. Therefore, methods that reduce threshold inconsistency are more likely to yield more repeatable and stable results under comparable conditions. Regarding *D. punctatus* pest monitoring, two key issues remain: (1) a lack of severity grading methods based on statistical optimization with good operability and repeatability, and (2) insufficient mining

of the progressive degradation information contained in time-series remote sensing features. Therefore, it is necessary to develop a quantitative severity classification method for *D. punctatus* pests that integrates multi-temporal remote sensing features, thereby achieving more refined and reliable monitoring of forest health status.

The adoption of machine learning algorithms has significantly enhanced the capabilities of remote sensing monitoring [42]. Algorithms such as Random Forest (RF) and Support Vector Machine (SVM) can effectively handle nonlinear relationships in high-dimensional feature spaces. Bhattarai et al. [43] compared RF, SVM, and Multilayer Perceptron (MLP) for forest defoliation detection and found that RF consistently outperformed the other methods across multi-resolution datasets. RF efficiently processes high-dimensional features through ensemble learning and requires relatively small training sample sizes [44,45]. It is widely recognized as a robust classifier in remote sensing applications, often matching or exceeding SVM in terms of accuracy and stability across diverse land cover mapping tasks. For example, in coarse-resolution land cover mapping, RF achieved higher classification accuracy and better handling of mixed classes than SVM [46]. Meta-analyses further indicate that RF generally delivers stable performance across various applications and spectral settings while requiring relatively minimal parameter tuning [47]. Although SVM achieves nonlinear classification via optimal hyperplanes and performs well in complex spectral recognition tasks [48], its effectiveness is highly sensitive to parameter selection, and its computational demands are significantly higher [49]. In contrast, RF combines high accuracy with practical engineering advantages, and particularly excels in processing medium-scale remote sensing datasets. Although deep learning methods such as Convolutional Neural Networks (CNN), Long Short-Term Memory (LSTM) networks, and attention-based or Transformer-inspired models have achieved remarkable progress in feature extraction and time-series modeling for satellite imagery [50–53], their effective deployment often requires large-scale labeled datasets and substantial computational resources. Considering the data availability, computational constraints, and the need for interpretable and operationally feasible models in this study, we selected Random Forest (RF) as the core modeling method. This choice enables us to maintain high predictive accuracy while ensuring enhanced transparency and ease of deployment.

Given the challenges in current research on forest pest monitoring, including limited temporal scope, high subjectivity in classification systems, and inadequate use of sequential characteristics, this study focuses on the *D. punctatus* infestation in Qianshan City. It employs time-series Sentinel-2 multi-band images from 2019 to 2024. A monthly scale monitoring model was developed, integrating spectral data, vegetation indices, terrain features, meteorological information, and temporal sequences. The primary innovations of this research are as follows:

- A classification standard for the severity of *D. punctatus* infestation was established. The Weighted Composite Index (WCI) is computed using a logistic regression model, and the Gaussian kernel density method is applied to minimize the overlap between healthy and infested samples, thereby facilitating a quantitative classification of disaster severity.
- This study extracted temporal features across four dimensions: temporal volatility, trend, extreme value characteristics, and decline rate. Notably, the peak slope feature effectively describes the transition of vegetation from the growth phase to the decline phase, thereby providing a more comprehensive reflection of pest dynamics.
- A random forest-based model was developed for monitoring *D. punctatus* infestation severity. The multi-temporal sampling strategy spanning multiple years and months enhanced model robustness and generalization across diverse phenological stages.

This study aims to establish a scientific and scalable time-series remote sensing monitoring framework for *D. punctatus*, offering data support and methodological guidance for the ecological security assessment and monitoring of pest and disease infestation in southern pine forests.

2. Materials and Methods

2.1. Study Area

Qianshan City (30°27′–31°04′N, 116°14′–116°46′E) is situated in the southwestern region of Anhui Province, China, at the southern base of the Dabie Mountains (Figure 1). This area exhibits a typical subtropical monsoon climate, with an average annual temperature of 15.8 °C and annual precipitation ranging from 1300 to 1500 mm [54]. These favorable climatic and hydrological conditions create an optimal environment for the growth of *Pinus massoniana Lamb* [55]. Influenced by topography and climate, the region is extensively covered by pure *Pinus massoniana* forests and pine–broadleaf mixed forests at elevations between 300 and 800 meters. This expansive contiguous forest area facilitates the proliferation of *D. punctatus* populations.

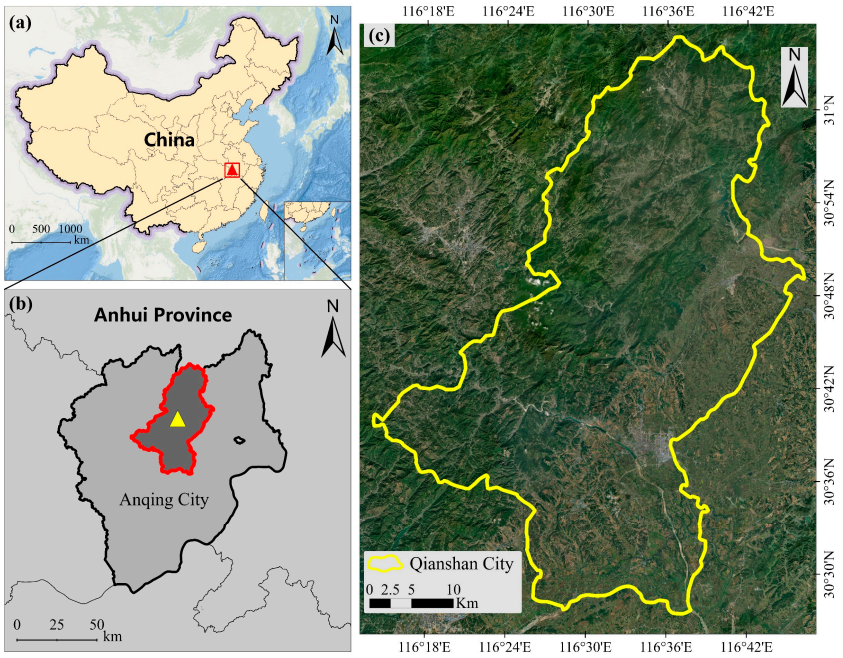


Figure 1. (**a**) The geographic location of Anhui Province within China. The map is based on a standard map (Approval No. GS (2024)0650) from the Department of Natural Resources Standard Map Service website, without any modification to the original boundaries; (**b**) The location of Anqing City, Anhui Province; (**c**) The location of Qianshan City, shown on a base map sourced from MAPWORLD imagery, where the yellow solid line denotes the study area boundary.

D. punctatus is among the most destructive defoliating pests in southern China. The larvae feed in large aggregations, resulting in significant leaf loss over a brief period [56]. During severe infestation, entire pine forests may succumb, leading to considerable ecological and economic impacts [57]. Qianshan City in Anhui Province has experienced frequent infestation of *D. punctatus* from mid-May to late September due to its favorable climate and abundant host resources, making it an important area for pest monitoring. To ensure completeness of the time-series analysis, remote sensing data were collected from April to October. The monitoring results, however, primarily focus on June to September, which corresponds to the peak infestation period when spectral responses are most pronounced.

2.2. Data Acquisition and Preprocessing

2.2.1. Remote Sensing Imagery

This research utilized Sentinel-2 and China's Gaofen-1/2 (GF-1/2) satellites as the primary sources of remote sensing data for tracking *D. punctatus* infestation. Sentinel-2 offers 13 spectral bands covering visible light to shortwave infrared, with spatial resolutions of 10 m, 20 m, and 60 m, and a revisit cycle of 5 days [58]. The data employed in this study were Level-2A (L2A), which had been corrected for atmospheric and topographic effects, making them directly suitable for surface analysis and quantitative applications [59]. To fulfill the monitoring needs on a monthly scale, cloud-free Sentinel-2 Level-2A reflectance composite images were acquired for the timeframe spanning from April to October annually from 2019 to 2024 within the research area. Given that *D. punctatus* infestations predominantly occur between late May and early September each year [60], the chosen period (April–October) ensured comprehensive coverage of the entire infestation process, which was vital for precise monitoring of pest dynamics. The composite images were created utilizing eight spectral bands: blue (B2), red (B4), red-edge (B5, B6, and B7), near-infrared (B8), and shortwave infrared (B11 and B12), all resampled to a consistent spatial resolution of 10 m × 10 m.

The GF-1 and GF-2 satellites are integral components of China's high-resolution Earth observation system (CHEOS), significantly contributing to national land resource monitoring [61]. Both satellites are equipped with blue, green, red, and near-infrared bands. GF-1 features multispectral bands with a spatial resolution of 8 m, while its panchromatic band achieves a resolution of 2 m. In contrast, GF-2 offers multispectral bands at a resolution of 4 m and a panchromatic band with a resolution of 1 m. In this study, GF-1/2 data were processed using pan-sharpening [62] in ENVI 5.3 to generate high-resolution fused data, which served as a reference for the visual interpretation of sample selection.

2.2.2. Topographic, Meteorological, and Land Cover Data

Topographic data encompassed a digital elevation model (DEM), slope, and aspect. The DEM data were acquired from the ALOS (Advanced Land Observing Satellite-1) project of Japan's Aerospace Exploration Agency (JAXA) at a spatial resolution of 12.5 m, accessible via the ASF Data Portal (https://asf.alaska.edu, accessed on 13 May 2025). Slope and aspect were derived using a 3 × 3 pixel window from the DEM. All topographic data (DEM, slope, and aspect) were subsequently resampled to a consistent spatial resolution of 10 m × 10 m.

Meteorological data were obtained from the open data platform (https://www.tpdc.ac.cn/, accessed on 22 August 2025), which included monthly precipitation, average temperature, potential evapotranspiration, and maximum and minimum temperatures from 2019 to 2024. Following spatial interpolation, all meteorological variables were resampled to a 10 m × 10 m resolution.

Land cover data were extracted from the high-precision global land cover dataset (GLC_FCS10) published by Liu et al. [63] (https://zenodo.org/records/14729665, accessed on 5 September 2025), which is also maintained a resolution of 10 m.

To align with the infestation environment of *D. punctatus*, the difference in the normalized difference vegetation index (NDVI) between the vegetation growing season and leaf-fall period in the same year was calculated. This analysis facilitated the identification and extraction of pine forest distribution. The pine forest distribution map was then used as a mask to restrict monitoring exclusively to pine-dominated areas.

2.3. Methodology

This study developed a quantitative monitoring method for *D. punctatus* infestation using time-series multi-source data. Figure 2 illustrates the entire workflow, which primar-

ily comprises five components: Sentinel-2 cloud-free image synthesis, Weighted Composite Index (WCI) construction, sample extraction, feature construction, and model training and validation. Monthly cloud-free composite images from Sentinel-2 served as the primary data source for this process. The WCI was developed to provide preliminary stratification of damage severity to guide sample selection. High-resolution GF-1/2 imagery facilitated visual interpretation, enabling the generation of sample sets categorized into healthy, light, moderate, and severe damage classes. The WCI was solely used for sample labeling and was not included as a model input feature. The model inputs comprised spectral data, vegetation indices, topographic data, meteorological variables, and features representing temporal dynamics. The final model was trained using the RF algorithm, and its performance was evaluated using confusion matrices.

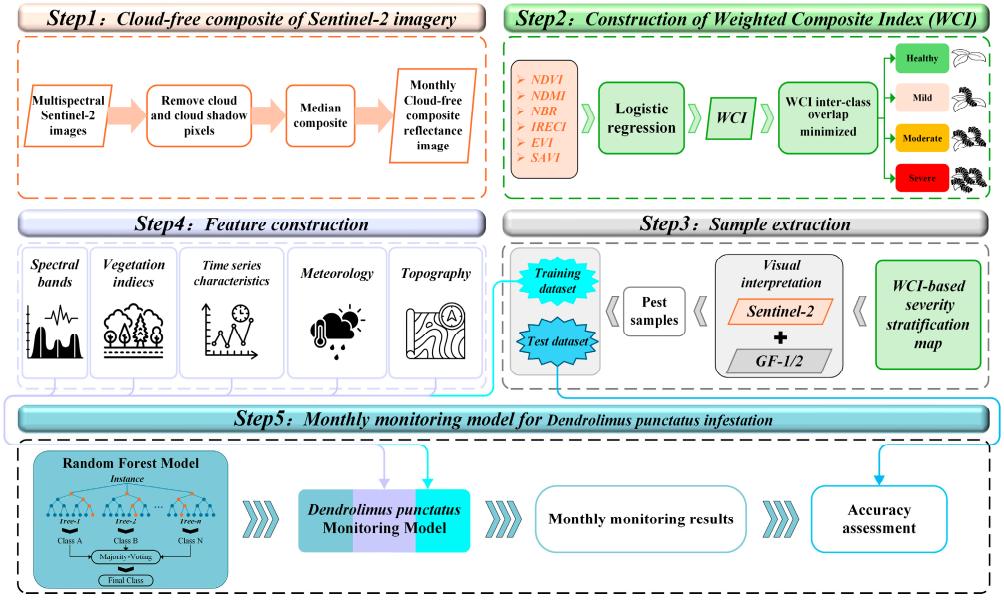


Figure 2. Overall technical workflow for monthly monitoring of *D. punctatus* infestation severity.

2.3.1. Sentinel-2 Monthly Data Composite

This study focused on the primary infestation period of *D. punctatus* from June to September annually during 2019–2024. Cloud-free Sentinel-2 Level-2A imagery with less than 30% cloud cover was chosen for the study area through the Google Earth Engine (GEE) platform. Monthly composite images were created for each month by combining all available imagery using a median compositing method to reduce the influence of clouds, atmospheric effects, and outliers [64]. The formula for generating the monthly composite image is as follows:

$$I_m(x,y) = median\{I_i(x,y) \mid I_i(x,y) \in M_m\} \quad (1)$$

where $I_m(x,y)$ represents the reflectance value of the composite image for month m at pixel (x,y); $I_i(x,y)$ represents the corresponding pixel reflectance of the i-th valid Sentinel-2 image in month m; and M_m is the set of all images in month m that satisfy the cloud cover condition.

Consequently, cloud-free monthly composite images spanning 2019–2024 were generated, offering high-quality time-series data for subsequent pest surveillance and vegetation index computation.

2.3.2. Classification of *D. punctatus* Damage Levels

Pest feeding on pine needles damages the canopy structure, resulting in vegetation wilting and a decrease in leaf water content [65]. The red band reflectance increases, while reflectance in the near-infrared and red-edge bands decreases, and the absorption characteristics in the shortwave infrared band are enhanced [66].

To comprehensively capture these pest-induced canopy responses, an initial set of 24 widely used vegetation indices was constructed based on Sentinel-2 spectral bands, covering vegetation greenness, chlorophyll content, moisture status, structural disturbance, and soil background effects. All candidate indices were evaluated using a unified sample set and comparison framework to assess their capability in discriminating between pest-affected and healthy pine forests. Through this screening process, six vegetation indices demonstrating the strongest and most stable sensitivity to pine caterpillar infestations were selected as inputs for the WCI. Specifically, NDVI and EVI were used to characterize overall vegetation greenness and canopy vigor, offering improved sensitivity under high-biomass forest conditions. IRECI was included to represent variations in chlorophyll content and red-edge responses, which are particularly sensitive to early physiological stress. NDMI was employed to quantify changes in canopy moisture status, reflecting reductions in leaf water content caused by pest infestation. NBR was incorporated to capture canopy structural disturbance, as it is highly responsive to changes in near-infrared and shortwave infrared reflectance. Additionally, SAVI was used to mitigate soil background effects, which become more pronounced under partial canopy loss.

Collectively, these indices provide a complementary and physically interpretable representation of pest-induced changes in forest canopy condition. All indices were calculated using cloud-free monthly composite Sentinel-2 imagery, and their formulations are summarized in Table 1.

Table 1. Shows the vegetation indices used in this study.

Vegetation Index	Equation	Reference
Normalized Difference Moisture Index (NDMI)	$(\rho_{NIR} - \rho_{SWIR1}) \ / \ (\rho_{NIR} + \rho_{SWIR1})$	[67]
Infrared Red Edge Chlorophyll Index (IRECI)	$(\rho_{Red\ Edge\ 3} - \rho_{Red}) \times \rho_{Red\ Edge\ 2} \ / \ \rho_{Red\ Edge\ 1}$	[68]
Soil-Adjusted Vegetation Index (SAVI)	$1.5\ (\rho_{NIR} - \rho_{Red}) \ / \ (\rho_{NIR} + \rho_{Red} + 0.5)$	[69]
Normalized Difference Vegetation Index (NDVI)	$(\rho_{NIR} - \rho_{Red}) \ / \ (\rho_{NIR} + \rho_{Red})$	[70]
Enhanced Vegetation Index (EVI)	$2.5\ (\rho_{NIR} - \rho_{Red}) \ / \ (\rho_{NIR} + 6\ \rho_{Red} - 7.5\ \rho_{Blue} + 1)$	[71]
Normalized Burn Ratio (NBR)	$(\rho_{NIR} - \rho_{SWIR2}) \ / \ (\rho_{NIR} + \rho_{SWIR2})$	[72]

To quantitatively delineate forest damage severity, six vegetation indices—NDVI, EVI, NBR, IRECI, NDMI, and SAVI—were selected as input variables for constructing the WCI. A logistic regression model with L1 regularization [73] was first applied to evaluate the contribution of each vegetation index in distinguishing healthy from infested stands. The resulting regression coefficients were normalized and used as weighting factors in the weighted summation of the indices. Subsequently, Gaussian Kernel Density Estimation (KDE) was applied to the WCI values derived from both healthy and infested samples in the training dataset. The classification thresholds for dividing the WCI into four severity levels were determined based on the intersection points of the probability density curves, specifically where overlap between the healthy and infested distributions was minimized. This data-driven approach enhances class separability while avoiding arbitrary threshold selection.

Training and validation samples were obtained through field surveys assisted by unmanned aerial vehicles (UAVs). Typical plots were first identified using UAV imagery, followed by manual visual interpretation of high-resolution GF-1/2 and Sentinel-2 images

to classify the severity of infestation for each year. This multi-scale sampling procedure ensured that the thresholds reflect both observed forest conditions and regional characteristics, thereby supporting the biological significance and operational applicability of the proposed severity classification framework.

(1) Standardization

To mitigate the effects of varying numerical scales among different vegetation indices, all input features were standardized prior to weight determination. Here, $i = 1, \ldots, N$ denotes the sample index, and $j = 1, \ldots, n$ denotes the vegetation index, where $N = 1120$ corresponds to 280 samples for each of the four damage classes (healthy, slightly infested, moderately infested, and severely infested), and $n = 6$ is the number of vegetation indices. Let X_{ij} denote the value of the j-th vegetation index for the i-th sample. The standardized value Z_{ij} is calculated as:

$$Z_{i\,j} = (X_{i\,j} - \mu_j)/\sigma_j \tag{2}$$

where X_{ij} represents the original index value, and μ_j and σ_j represent the mean and standard deviation of the j-th vegetation index, respectively, computed over the entire training sample set. This standardization ensures consistent feature scaling across different vegetation indices and provides a unified input space for subsequent modeling.

(2) Weight Determination

A logistic regression model with L1 regularization was employed to quantify the contribution of each vegetation index. The multi-class damage labels were binary-encoded as 0 for healthy samples and 1 for infested samples (including slightly, moderately, and severely infested), so that the model captures the distinction between healthy and damaged canopies. The probability of sample i being classified as infested, $P(y_i = 1)$, is expressed as:

$$P(y_i = 1) = \frac{1}{1 + e^{-(\beta_0 + \sum_{j=1}^{n} \beta_j Z_{i\,j})}} \tag{3}$$

where Z_{ij} is the standardized value of the j-th vegetation index for sample i, β_0 is the intercept, and β_j is the regression coefficient for the j-th index. The L1 penalty encourages sparsity in β_j, highlighting indices with greater discriminatory power.

The normalized weights W_j for constructing the WCI were obtained as:

$$W_j = \frac{|\,\beta_j\,|}{\sum_{k=1}^{n} |\beta_k\,|} \tag{4}$$

(3) Computation of the Weighted Composite Index

Utilizing the normalized weights, the WCI for the i-th sample was computed.

$$WCI_i = \sum_{j=1}^{n} W_j Z_{i\,j} \tag{5}$$

where W_j reflects the relative contribution of each vegetation index to distinguishing infested from healthy samples, and WCI_i represents the overall severity of *Dendrolimus punctatus Walker* infestation for sample i. A higher WCI value signifies increased levels of forest defoliation and canopy degradation, thereby indicating more severe infestation.

2.3.3. Sample Extraction

D. punctatus larvae primarily cause defoliation by feeding on the leaves, leading to a significant loss of foliage. From a remote sensing perspective, this phenomenon is reflected in fluctuations of various vegetation growth indices [74]. This study utilized WCI

classification results to stratify samples, categorizing forest stand conditions into four levels: healthy, mild, moderate, and severe. Given the significant inter-annual and intra-annual variability of *D. punctatus* infestation, samples were collected in June 2019, July 2020, August 2021, September 2022, August 2023, and June 2024. For each time-period, 400 samples were selected for each severity level, thereby constructing a multi-year, multi-month sample set for subsequent model training and validation. This design effectively captures spectral response differences across varying infestation severity levels while accounting for inter-annual fluctuations, thus enhancing the model's generalization capability.

2.3.4. Infestation Monitoring Model

(1) Input Features

This study developed a multi-dimensional feature system consisting of 34 indicators categorized into five groups: spectral features, vegetation indices, meteorological variables, topographic factors, and temporal features.

Spectral and vegetation index features were extracted from Sentinel-2 imagery to characterize canopy reflectance and assess the physiological status of vegetation. Meteorological and topographic features represented the environmental conditions influencing forest growth. Temporal features were derived from monthly EVI and IRECI series spanning April to October and included six indicators: standard deviation, cumulative change, average rate of change, extreme values (maximum/minimum), and peak slope. These indicators characterized the volatility, trends, extreme characteristics, and decline rates of vegetation health. The integration of temporal and static features created a "static-dynamic" feature system, offering multi-dimensional inputs for monitoring infestation.

Temporal standard deviation (S_t) quantified temporal volatility; healthy vegetation typically exhibited low volatility, whereas infested areas demonstrated increased fluctuations.

$$S_t = \sqrt{\frac{1}{n-1}\sum_{i=1}^{n}(x_i - \overline{x})^2} \quad (6)$$

Cumulative change (C_t) was calculated as the difference between the final and initial observations, representing the net variation in the vegetation index over the entire monitoring period. Healthy vegetation generally exhibits positive cumulative change, whereas pest infestation is typically associated with negative values as a result of sustained canopy degradation.

$$C_t = x_n - x_1 \quad (7)$$

The average rate (R_t) was calculated to characterize the overall intensity of *Dendrolimus punctatus Walker* infestation by normalizing the cumulative change in the index by the number of temporal intervals, thereby capturing the mean rate of change per time step. Under sustained *D. punctatus* infestation, continuous needle defoliation constrains canopy recovery and photosynthetic activity, resulting in persistently declining index values; consequently, infested pixels exhibit significantly lower R_t values than healthy stands.

$$R_t = \frac{x_n - x_1}{n-1} \quad (8)$$

Temporal extremes (MAX_t/MIN_t) indicated the peak and trough values observed during the growing season, with infested pixels typically displaying reduced peaks.

Peak slope (P_t) was calculated using linear fitting, where a valid peak ($\geq$3 observations) was used to determine the slope from the peak to the endpoint; otherwise, the complete time series was fitted. Figure 3 illustrates three typical cases of slope calculation based on IRECI, with blue solid lines depicting monthly variation curves and orange solid lines

representing the extracted slope segments. Here, IRECI is used solely as an illustrative example to demonstrate the slope extraction procedure.

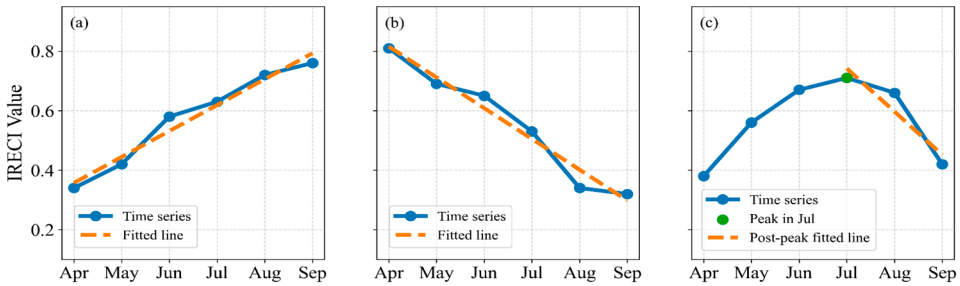


Figure 3. Three potential scenarios for slope extraction. (**a**) A monthly upward trend without a peak; (**b**) A monthly downward trend without a peak; (**c**) A curve fit determined post peak identification (July).

(2) Random Forest

This study employed the Random Forest algorithm as the core method for constructing the *D. punctatus* monitoring model. Random Forest, a non-parametric classification algorithm rooted in ensemble learning, mitigates overfitting and boosts model resilience by aggregating decisions from numerous trees [75]. To ensure the model's generalization ability and classification reliability during training and prediction, the samples were divided into 70% for training and 30% for validation.

2.3.5. Model Validation

The model's accuracy was assessed through confusion matrices [76]. The evaluation metrics were derived from the counts of True Positives (TP), False Positives (FP), True Negatives (TN), and False Negatives (FN) calculated from both the training and test sets. For the final performance assessment, 30% of the samples were randomly partitioned as an independent validation set to ensure an unbiased evaluation of the model's generalization capability. In this study, Precision and Overall Accuracy were employed to quantify the classification reliability and overall performance of the random forest model for *D. punctatus* infestation monitoring.

$$Precision = TP \,/\, (TP + FP) \tag{9}$$

$$Overall\ Accuracy = (TP + TN) \,/\, (TP + FP + TN + FN) \tag{10}$$

3. Results

3.1. Sentinel-2 Data Compositing and Vegetation Indices

The reflectance imagery and the responses of NDVI, NDMI, EVI, NBR, SAVI, and IRECI to *D. punctatus* infestation in typical sample areas based on cloud-free Sentinel-2 composites from August 2023 are shown in Figure 4a–d. As shown in the figure, infested areas (indicated by red circles) displayed notably low values in greenness-related indices (NDVI, EVI, SAVI, and IRECI), appearing as dark red, while healthy areas exhibited high values, shown as dark blue. Due to needle withering and defoliation caused by *D. punctatus* feeding, canopy water content in infested pine forests decreased significantly, resulting in low NDMI values in affected patches. NBR, which integrates near-infrared and shortwave infrared band information, also demonstrated sensitivity to vegetation moisture changes and desiccation, displaying low values in infested areas.

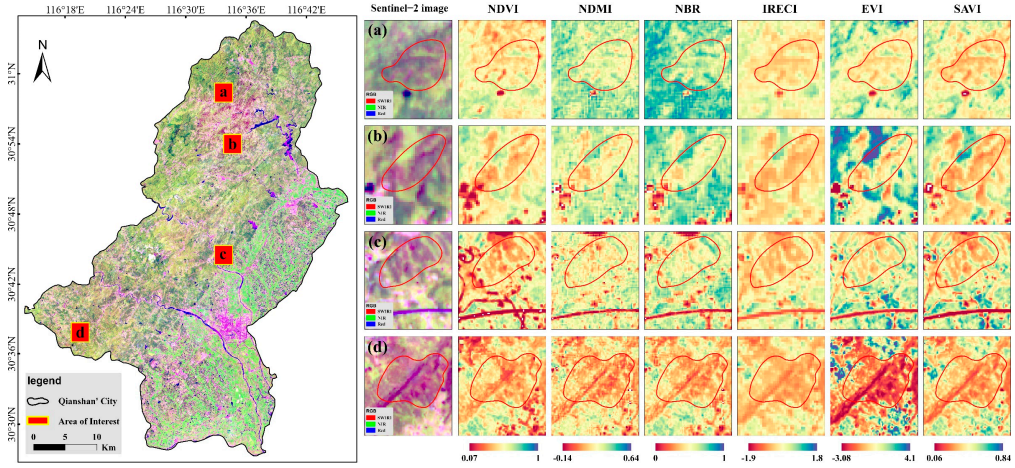


Figure 4. The image was created using a false color composite (RGB = SWIR1, NIR, Red). Four representative sample regions (**a**–**d**) were selected for localized magnification examination, illustrating areas affected by D. punctatus as observed in Sentinel-2 imagery and analyzed using multiple vegetation indices, including NDVI, NDMI, NBR, EVI, IRECI, and SAVI. (**a**) Zoomed-in view of representative region a; (**b**) Zoomed-in view of representative region b; (**c**) Zoomed-in view of representative region c; (**d**) Zoomed-in view of representative region d.

All six indices demonstrated strong spatial consistency across the four sample areas (a–d), with infested zones exhibiting low values while healthy areas maintained high values. The consistent response across multiple indices indicated that *D. punctatus* infestation had a comprehensive impact on vegetation greenness and canopy water content, while also reflecting the synergistic role of NDVI, NDMI, EVI, NBR, SAVI, and IRECI in identifying *D. punctatus* infestation.

3.2. Severity Classification of D. punctatus Infestation

The spectral curves for both healthy and infested pine forests are shown in Figure 5. Reflectance differences within the visible spectrum (492–704 nm) were relatively minor, whereas the most pronounced differences occurred in the red-edge region (704–864 nm). Healthy pine forest exhibited distinctly steep red-edge slopes, in contrast to the flattened slopes observed in infested pine forest. Significant differences in near-infrared reflectance indicated a reduction in leaf water content. In the water vapor absorption band at 945 nm and extending to the shortwave infrared region at 2185 nm, healthy pine forest demonstrated a more pronounced decline in reflectance. A comprehensive analysis revealed that the Red Edge 1–3, NIR, and SWIR1-2 bands were particularly sensitive to *D. punctatus* infestation, thereby supporting the scientific validity of employing NDVI, EVI, NBR, IRECI, NDMI, and SAVI for assessing infestation severity through remote sensing.

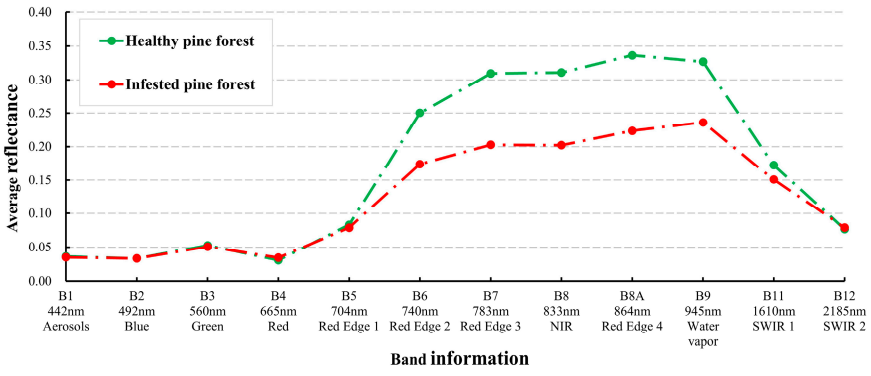


Figure 5. The spectral curves for both healthy and infested pine forest.

Figure 6a,b illustrate box plots and probability density distributions of six vegetation indices across varying levels of infestation severity. As infestation severity increased, the index values generally declined, indicating a reduction in vegetation greenness and vigor. IRECI, NBR, and NDMI exhibited the most significant distributional differences across severity levels; Figure 6c,d display box plots and probability density distributions for WCI. The distribution peaks for different severity levels were distinctly separated. The healthy category was concentrated at WCI < −0.56, the mild category ranged from −0.56 to 0.18, the moderate category spanned from 0.18 to 0.94, and the severe category was defined by WCI > 0.94. Although the healthy and mild categories showed slight overlap between −1 and 0, the moderate and severe peaks shifted distinctly to the right, indicating that WCI effectively differentiated between various infestation stages and achieved optimal separation among severity levels; Figure 6e presents the weight distributions of vegetation indices in WCI. EVI, NDVI, and IRECI exhibited higher weights, suggesting that WCI was primarily influenced by indicators related to chlorophyll content, canopy structure, and physiological activity; conversely, SAVI had a relatively lower weight but contributed supplementary soil background information.

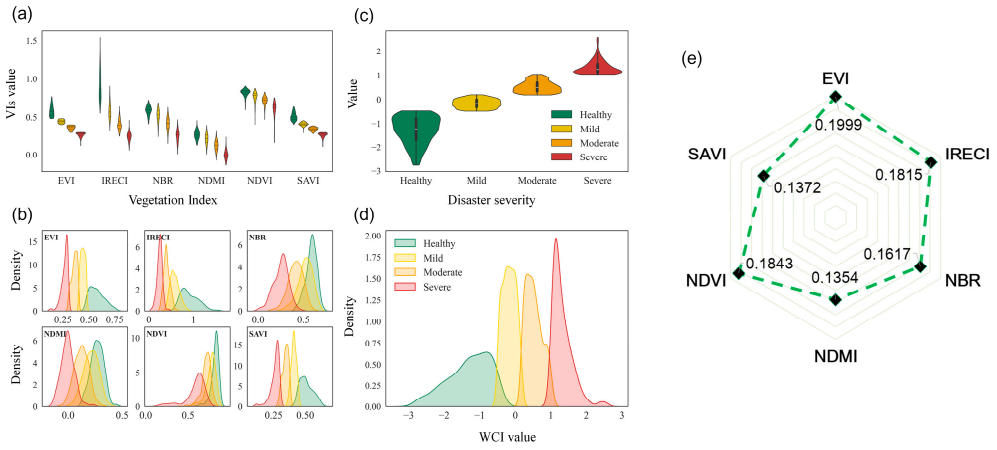


Figure 6. This figure presents the distribution characteristics and weight contributions of vegetation indices and the Weighted Composite Index (WCI). Panels (**a**,**b**) display box plots and probability density distributions of EVI, IRECI, NBR, NDMI, NDVI, and SAVI across various infestation severity levels. Panels (**c**,**d**) show box plots and probability density distributions of WCI at different infestation severity levels, while Panel (**e**) illustrates the weights assigned to each vegetation index in the WCI.

The distributional characteristics and weight results of WCI mutually confirmed that this index effectively quantified infestation severity, providing a basis for sample selection. Table 2 lists WCI thresholds for healthy, mild, moderate, and severe categories.

Table 2. WCI threshold classification criteria for healthy, mild, moderate, and severe severity levels.

Level	WCI Threshold Range
Healthy	[<−0.56]
Mild	[−0.56, 0.18]
Moderate	[0.18, 0.94]
Severe	[>0.94]

3.3. Sample Extraction Results

Utilizing the WCI threshold classification system, this study integrated multi-source remote sensing data from GF-2, GF-1, and Sentinel-2 to extract samples that ensured representativeness and consistency across temporal, spatial, and sensor dimensions. The samples encompassed peak infestation months of *D. punctatus* from 2019 to 2024, specifically

June 2019, July 2020, August 2021, September 2022, August 2023, and June 2024, thereby reflecting inter-annual and seasonal dynamics of infestation. Figure 7 illustrates the spatial distribution of samples and the imagery characteristics from different sensors.

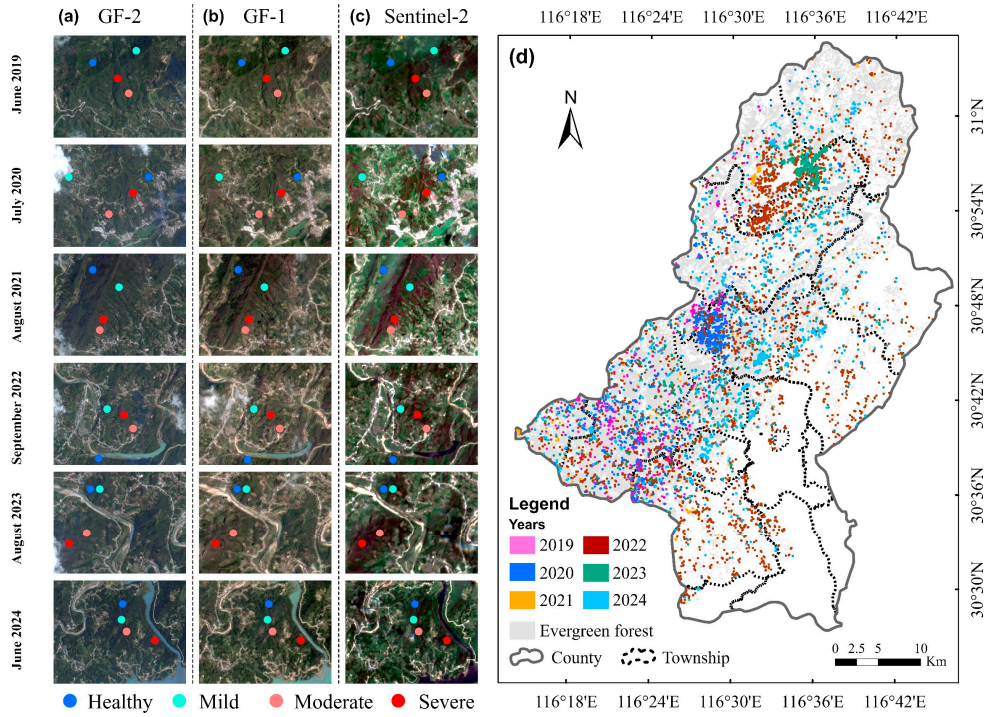


Figure 7. Spatial distribution and imagery comparison of *D. punctatus* infestation samples from multi-source remote sensing. (**a**) GF-2 true-color imagery for different acquisition periods; (**b**) GF-1 true-color imagery for different acquisition periods; (**c**) Sentinel-2 true-color imagery for different acquisition periods; (**d**) Overall spatial distribution of samples across the study area for different collection years.

Figure 7a–c display true color imagery from GF-2, GF-1, and Sentinel-2 for representative areas, accompanied by corresponding samples of varying severity levels, which were distinguished by color. Although the different sensors exhibited variations in spatial resolution, texture detail, and representation of forest stand structure, all effectively identified the spectral and canopy characteristics of both healthy and infested stands. This indicates that multi-source remote sensing data were complementary and provided extensive information for sample extraction; Figure 7d demonstrates that samples were evenly distributed across the study area, encompassing major forest types and peak infestation months across different years. This distribution illustrated good spatial and temporal representativeness, thereby establishing a data foundation for infestation monitoring and change analysis.

3.4. D. punctatus Monitoring Model and Feature Importance Analysis

The *D. punctatus* monitoring model employed a monthly input-output mode, constructing 34 indicators across five categories: spectral features, vegetation indices, meteorological features, topographic features, and temporal features.

Figure 8a illustrates feature importance in the random forest model for monitoring infestation severity. Vegetation indices demonstrated the highest contribution, with IRECI, NDVI, NBR, and NDMI ranking among the top four, reflecting their sensitivity to forest health degradation caused by pest damage. Temporal features derived from vegetation index time series, particularly regression slopes of EVI and IRECI, ranked second in importance, underscoring the value of phenological dynamics in characterizing infestation progression. Red-edge spectral bands contributed moderately, while meteorological and

topographic variables exhibited relatively low importance, though they provided contextual information on environmental conditions and spatial heterogeneity of the infestation.

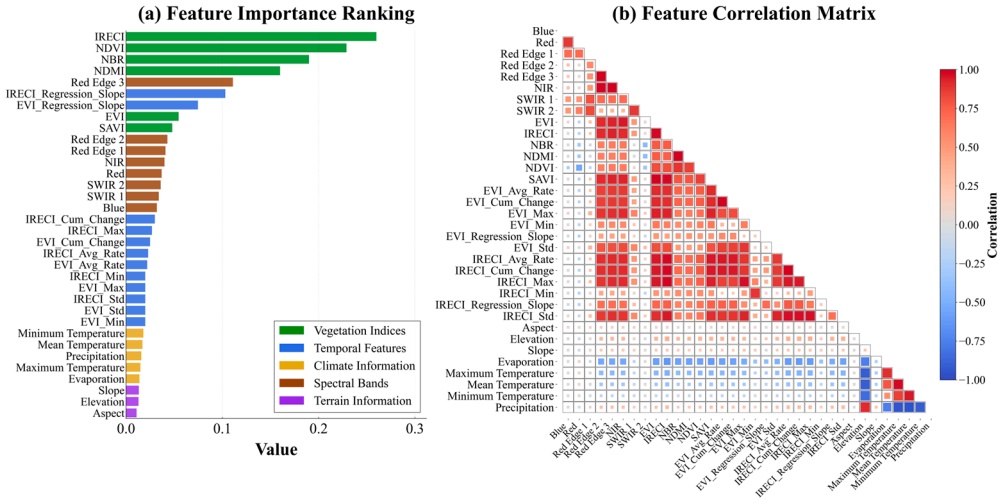


Figure 8. Correlation and feature importance analysis for *D. punctatus* monitoring. (**a**) Importance ranking of different feature categories in the model; (**b**) Correlation matrix of different feature categories in the model.

Figure 8b presents the feature correlation matrix. Strong positive correlations were observed among vegetation indices (EVI, IRECI, NDVI, NBR, NDMI, and SAVI) and between these indices and Red-Edge/NIR/SWIR bands, confirming that vegetation indices effectively integrate spectral information related to vegetation stress. Temporal features derived from the same index exhibited high intercorrelations, as expected given their shared mathematical basis. Conversely, meteorological variables, particularly evaporation, showed weak or negative correlations with spectral and vegetation features, while topographic variables (aspect, elevation, and slope) demonstrated minimal correlation with vegetation-related features.

These results reveal a hierarchical feature structure: vegetation indices serve as primary indicators of infestation severity, temporal dynamics provide complementary information on damage progression, and environmental variables contribute auxiliary spatial context for monitoring.

3.5. Monitoring Results and Accuracy Validation

The comprehensive monitoring results for the peak infestation months of *D. punctatus* from June to September between 2019 and 2024 are shown in Figure 9. The infestation severity in Masson pine forests demonstrated distinct temporal fluctuations. Throughout the study's duration, infestations were mainly observed in July, August, and September, exhibiting some inter-annual variability and periodic patterns. Particularly noteworthy were the infestation periods in July 2019, July 2020, July 2021, September 2022, August–September 2023, and June 2024. The infestation scale in 2019, 2021, and 2023 stood out significantly, surpassing that of other years.

Statistical analysis was performed on area changes across severity levels for June–September of each year to uncover temporal evolution patterns of *D. punctatus* infestation in Qianshan City (Figure 10). The monitoring results spanning from 2019 to 2024 revealed that infestations were predominantly concentrated in July, August, and September annually. Particularly, the years 2019, 2021, and 2023 stood out as major infestation years, with moderate severity areas averaging 843.4, 1023.8, and 993.5 ha, respectively, and severe areas averaging 1229.5, 978.7, and 1328.7 ha, respectively. Throughout the period of 2019–2024, healthy category areas exhibited an initial decrease followed by an increase,

and mild and moderate infestation ranges showed an expansion followed by contraction, whereas severe infestation areas peaked in 2023.

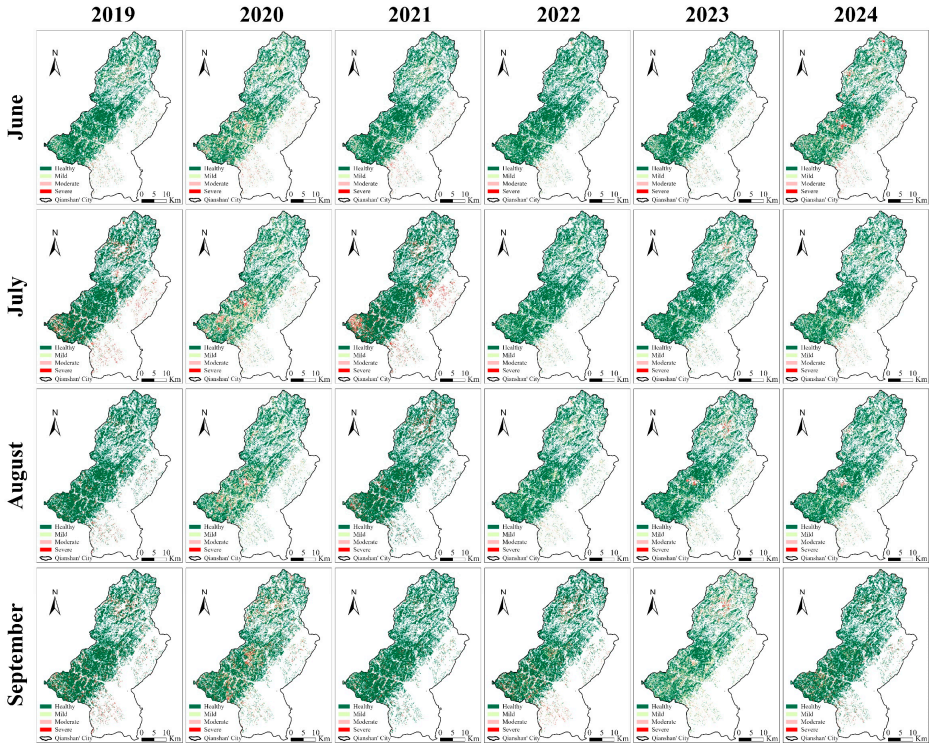


Figure 9. Overall monitoring results for peak infestation months of *D. punctatus* from 2019–2024.

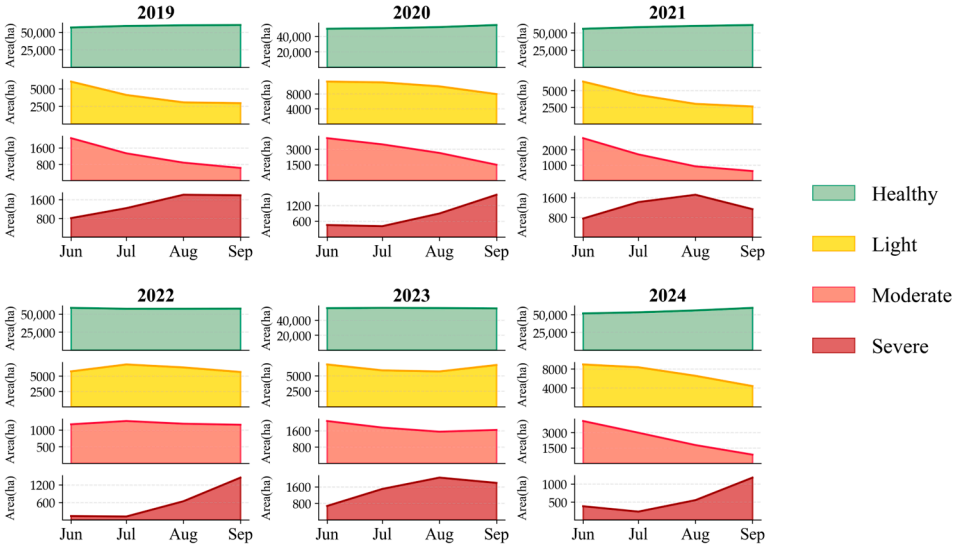


Figure 10. Statistical analysis of forest area changes across severity levels from 2019–2024. Infestation concentrated in July–September, with 2019, 2021, and 2023 being severe years.

Based on monitoring data from June to September annually, this research identified pixel types with the highest occurrence probability to create yearly composite outcomes and analyzed transitions among severity levels. Figure 11a–f illustrate the shifts in severity levels between 2019 and 2024. Healthy forests remained predominant but experienced shifts toward mild, moderate, and severe categories during peak infestation years, particularly 2019, 2021, and 2023. Mild infestation increased during infestation periods and partially reverted to healthy conditions or progressed to moderate levels. Moderate infestation primarily arose from transitions of healthy and mild areas, with a subset of pixels advancing

to severe levels. Severe infestation peaked in infestation years, mainly resulting from transitions from moderate infestation levels. Overall, approximately 10% of forested areas transitioned among mild and moderate categories over the study period, whereas severe infestation exhibited a general declining trend.

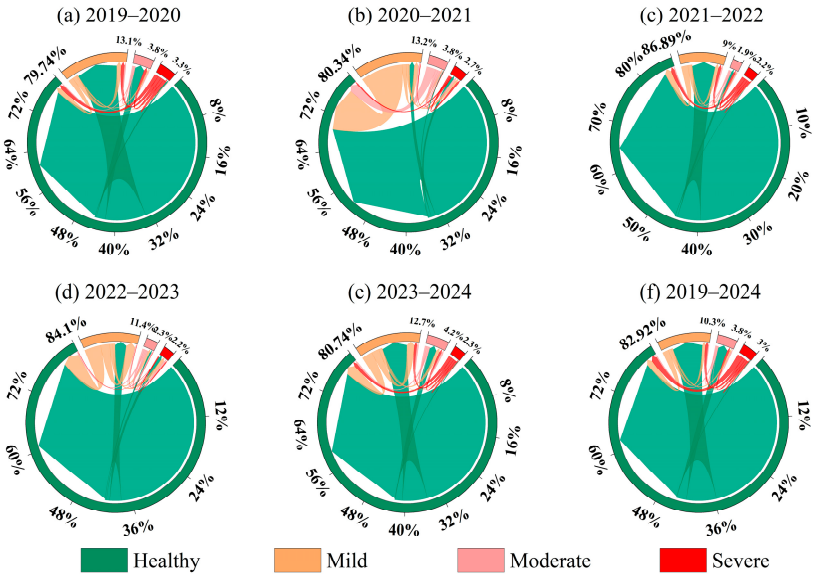


Figure 11. Transition analysis among *D. punctatus* severity levels from 2019–2024. (**a**) 2019–2020 severity-level area transitions; (**b**) 2020–2021 severity-level area transitions; (**c**) 2021–2022 severity-level area transitions; (**d**) 2022–2023 severity-level area transitions; (**e**) 2023–2024 severity-level area transitions; (**f**) Overall severity-level transition patterns (2019–2024).

Detailed views of the typical areas in June–September 2019 are presented in Figure 12. The infestation in that year was predominantly mild, with limited occurrences of moderate and severe damage. The mild infestation gradually expanded from June to September, primarily concentrated in parts of Huangbai Town, Doumu Town, and Huangpu Town. This pattern suggested that the *D. punctatus* infestation in 2019 was in its early stages, with affected areas displaying scattered distribution and significant spatial dispersion.

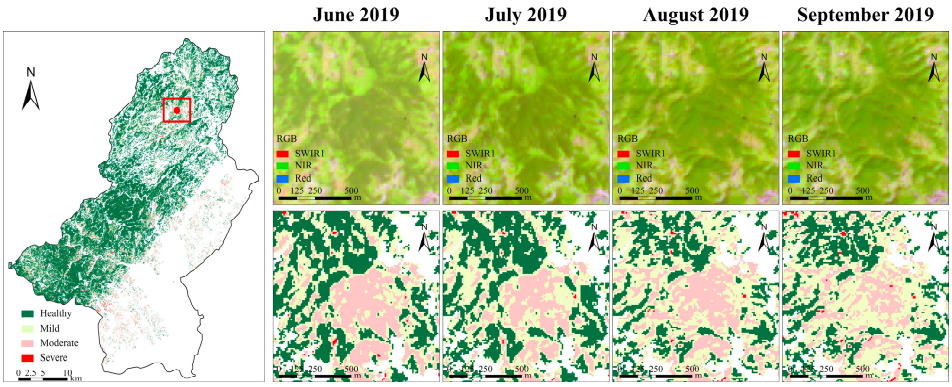


Figure 12. Detailed views of *D. punctatus* infestation in typical areas for 2019 (June–September).

Figure 13 presents detailed views of typical areas from June to September 2021. Beginning in June 2021, the intensity of infestation increased monthly, leading to a rapid expansion of affected areas. By September, most forest regions exhibited mild to moderate infestation, indicative of a high density of *D. punctatus* populations and regional spread across multiple townships within the study area. Furthermore, the simplistic structure of forest stands and an extended absence of regeneration may have created an environment conducive to the reproduction and dispersal of *D. punctatus*.

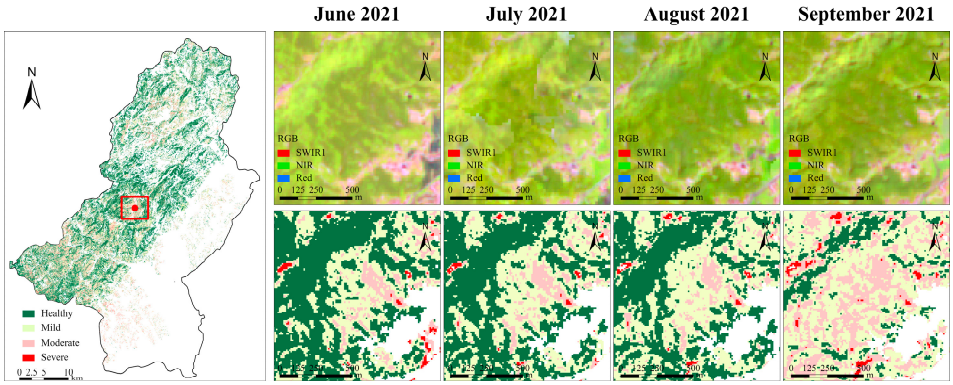


Figure 13. Detailed views of *D. punctatus* infestation in typical areas for 2021 (June–September).

Figure 14 illustrates detailed views of typical areas from June to September 2023. In 2023, infestation originated locally in June and developed into extensive affected areas by August, primarily concentrated in northern Qianshan City, including Huangbai Town, Tafan Township, and Chashui Town, as well as portions of Doumu Township and Huangpu Town. Analyzing temporal changes revealed that *D. punctatus* infestations were closely associated with the phenological development stages of pine trees. Each year, during May and June, *D. punctatus* larvae entered their peak feeding period, resulting in rapid infestation propagation in early summer. From July to September, as temperatures continued to rise and larvae further developed, forest damage intensified, with both the extent and intensity of infestation increasing concurrently.

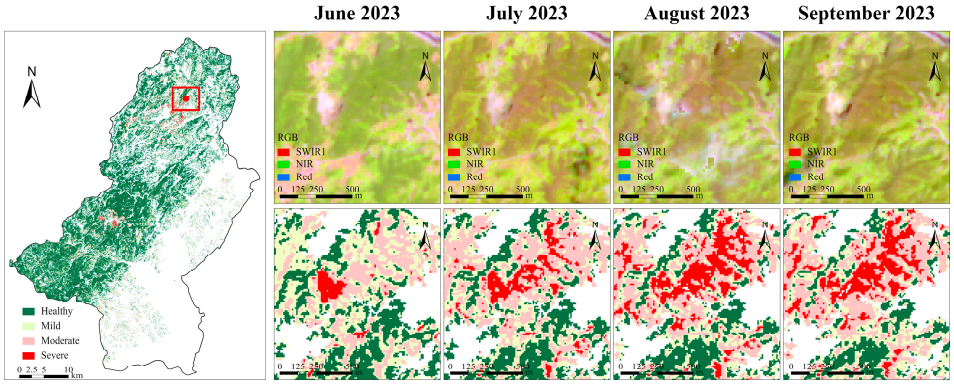


Figure 14. Detailed views of *D. punctatus* infestation in typical areas for 2023 (June–September).

The confusion matrices and accuracy assessments of the *D. punctatus* monitoring model for June 2019, July 2020, August 2021, September 2022, August 2023, and June 2024 are presented in Figure 15, corresponding to the sample extraction periods. These months capture spectral variations across infestation severities and inter-annual fluctuations, supporting model generalization. Overall accuracy ranged from 86.9% to 92.5%, with Kappa coefficients between 0.825 and 0.858, indicating reliable classification performance. Healthy forests were classified with the highest and most consistent accuracy, with 102–112 correctly classified samples and minimal commission and omission errors. Mild and moderate infestation had 101–108 correctly classified samples, with some confusion between adjacent categories. Severe infestations were mostly correctly classified, with 104–114 samples correctly identified and occasional misclassification as moderate, while maintaining low commission errors. Misclassifications predominantly occurred between adjacent severity levels, with minimal confusion between the extreme categories, demonstrating that the model effectively distinguishes the severity of *D. punctatus* infestation.

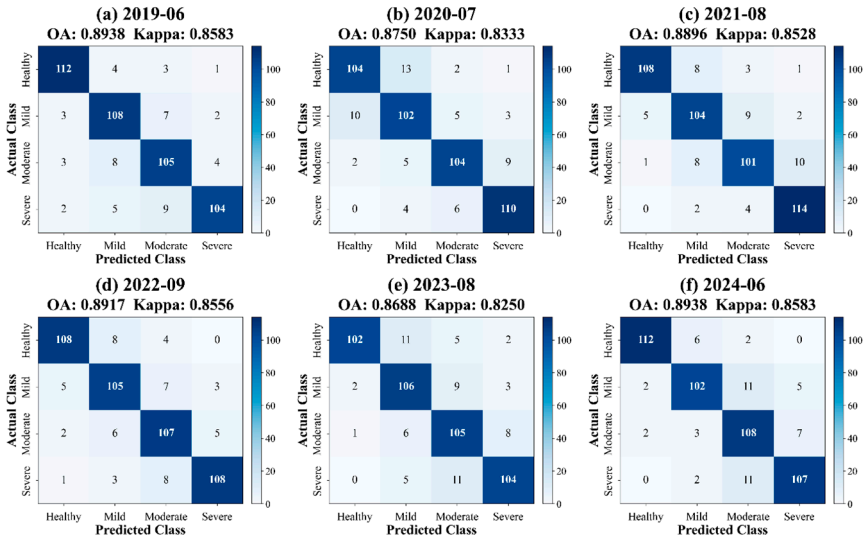


Figure 15. Confusion matrix analysis and accuracy results of *D. punctatus* monitoring model for different time periods: (**a**) June 2019, (**b**) July 2020, (**c**) August 2021, (**d**) September 2022, (**e**) August 2023, and (**f**) June 2024.

4. Discussion

4.1. Role of Multi-Source and Multi-Scale Data Fusion in Pest Sample Extraction

In the sample construction stage, this study employed high-resolution GF-1/2 imagery for visual interpretation, complemented by monthly median composites of Sentinel-2 data to generate training samples, thereby achieving an effective balance between spatial and temporal resolution. This strategy enhanced the representativeness and temporal consistency of the samples.

Recent studies have emphasized that multi-source data fusion has become a key direction in forest pest monitoring. For example, Illarionova et al. [77] developed a data fusion approach combining high-resolution imagery from Google Earth with medium-resolution Sentinel-2 data for monitoring boreal forests damaged by *Polygraphus proximus*. Their methodology demonstrated that high-resolution imagery facilitates precise identification of individual damaged trees, while Sentinel-2's multispectral bands enable large-scale disease classification through machine learning models. Similarly, Wulder et al. [78] used multi-date Landsat imagery along with elevation and solar-radiation surfaces to map mountain pine beetle red-attack damage in mixed-forest terrain, achieving an overall accuracy of 86%. Similarly, Liu et al. [79] found that high-resolution optical imagery facilitates precise delineation of sample boundaries, whereas medium-resolution time-series data capture seasonal dynamics more effectively. The multi-temporal sample system developed in this study covers the period from 2019 to 2024, integrating both spatial and temporal advantages, and provides a viable technical pathway for high-frequency monitoring of *D. punctatus* infestation.

4.2. Sensitivity of Vegetation Indices and the Remote Sensing Mechanism of the WCI

Results indicate that the red-edge (RE1–RE3), NIR, and SWIR bands exhibit the most pronounced spectral responses to *D. punctatus* damage. Affected samples show reduced reflectance slopes in the red-edge region (704–864 nm), a marked decline in NIR reflectance, and enhanced SWIR absorption. Similar findings were reported by Xu et al. [80], who observed that red-edge and NIR wavelengths effectively capture canopy structural degradation and loss of vegetation vigor, thus serving as critical spectral regions for the detection of *D. punctatus* pests. Additionally, Hais et al. [81] demonstrated that the NDMI is particularly

sensitive during the stages of needle desiccation, facilitating effective discrimination among various phases of damage.

The WCI developed in this study determines multi-index weights through logistic regression, with EVI, NDVI, and IRECI contributing most strongly to capturing canopy greenness and red-edge dynamics. This approach mitigates the influence of soil and atmospheric backgrounds on individual indices, thereby improving the stability of damage-level classification. Compared with recent studies that utilize multiple independent vegetation indices and require complex machine learning models for severity classification [82], the WCI provides a unified composite metric that synthesizes multi-dimensional spectral characteristics into a single interpretable value. This substantially reduces input complexity while maintaining high discriminative power. Furthermore, conventional approaches often employ multi-step processes, such as first estimating biophysical parameters like needle water content and then classifying severity based on measured thresholds [83]. In contrast, the WCI directly establishes a quantitative relationship between spectral features and infestation severity through logistic regression. The use of Gaussian Kernel Density Estimation to determine optimal classification thresholds ensures statistically rigorous and objective severity delineation [84], avoiding the subjective threshold selection common in traditional methods. This methodological contribution offers a streamlined, reproducible framework that is particularly valuable for operational forest management, where computational efficiency and model interpretability are critical.

Previous studies have shown that multi-index weighting can increase classification accuracy by 5–12% during early infestation stages [85]. Nevertheless, the WCI thresholds remain region-dependent and require recalibration when applied to other geographic or forest conditions to ensure model robustness.

4.3. Role and Limitations of Temporal Features in Characterizing the Infestation Process

Temporal derivatives of EVI and IRECI were incorporated into the model to complement static spectral features in describing forest dynamic changes. Feature importance analysis shows that temporal slopes ranked just below vegetation indices and were substantially more influential than meteorological and topographic variables, indicating that vegetation index trajectories effectively capture the spread dynamics of *D. punctatus* infestation. However, the reliability of temporal features depends on continuous, high-quality observations. Although the median composite strategy within the GEE platform alleviated cloud contamination, data gaps remained in some months. Moreover, while monthly composites enhance data availability and consistency, they also smooth short-term variations, potentially weakening sensitivity to subtle changes during the early infestation stages.

Future research should integrate higher-temporal-resolution multi-source datasets or apply time-series reconstruction algorithms to improve the stability and responsiveness of temporal indicators.

4.4. Advantages and Limitations of the Monthly Monitoring Model

Based on monthly cloud-free Sentinel-2 composites data, this study established a continuous monitoring model for *D. punctatus* from 2019 to 2024. The model achieved an overall accuracy exceeding 86.9%, with Kappa coefficients ranging from 0.825 to 0.858. Similar temporal compositing approaches have proven effective in large-scale vegetation index modeling [86]. The model exhibited the highest accuracy in distinguishing healthy and severely damaged stands, while misclassification mainly occurred in mildly affected samples, likely because canopy structural and spectral changes were not yet pronounced enough to differentiate them from healthy stands. Additionally, the spectral heterogeneity of mixed forests contributed to classification uncertainty.

Meteorological and topographic features showed relatively low importance, which may be attributed to the coarse spatial resolution (1 km) of meteorological data. Topographic variables primarily influence pest occurrence indirectly through modulation of light, moisture, and temperature gradients, and thus have weaker associations with canopy spectral responses. Nevertheless, retaining these factors aids in describing the environmental background and spatial heterogeneity of pest distribution, providing contextual support for interpreting regional infestation patterns.

Future studies should maintain the stability of monthly composites while incorporating radar or high-temporal-resolution optical imagery to further enhance the dynamic monitoring capacity and generalization performance of the model.

5. Conclusions

This study developed a Random Forest model for monthly monitoring of *D. punctatus* infestation using cloud-free Sentinel-2 composites (2019–2024), complemented by visually interpreted GF-1/2 imagery as reference samples. The model integrates spectral, vegetation index, meteorological, topographic, and time-series features. Results demonstrate that the proposed Weighted Composite Index (WCI) effectively discriminates among healthy, slightly damaged, moderately damaged, and severely damaged stands, achieving overall accuracies exceeding 86.9% and Kappa coefficients of 0.825–0.858 on validation datasets, thereby confirming the method's reliability for regional-scale pest monitoring. Key findings include:

- Combining high-resolution GF-1/2 imagery with medium-resolution Sentinel-2 composites and sampling across the main infestation period balances spatial detail with temporal continuity, enhancing dataset representativeness and enabling comprehensive characterization of infestation dynamics.
- The WCI synthesizes multiple vegetation indices, with EVI, NDVI, and IRECI receiving the highest weights to capture canopy greenness, growth vigor, and red-edge characteristics. This composite index provides a scientifically grounded and quantitative basis for discriminating damage severity levels, reducing reliance on subjective threshold selection.
- By integrating spectral, vegetation index, meteorological, topographic, and temporal features into the Random Forest model, this study establishes an effective continuous monthly monitoring approach. The framework reveals spatial spread patterns and the severity evolution of *D. punctatus* from 2019 to 2024, which are critical for understanding infestation trajectories and informing timely management interventions.

This work advances regional-scale pest monitoring by integrating multi-source data, synthesizing spectral information through the WCI, and constructing a temporally informed machine learning framework, thereby offering both methodological innovation and practical applicability for forest health assessment.

Author Contributions: Conceptualization, F.M.; methodology, F.M.; software, F.M.; validation, F.M. and X.Q.; formal analysis, F.M.; investigation, F.M., X.Q., Y.S., X.H. and F.J.; resources, F.M., X.Q. and Y.S.; data curation, F.M.; writing—original draft preparation, F.M.; writing—review and editing, F.M.; visualization, F.M., X.Q. and Y.S.; supervision, X.Q., Y.S., S.H. and L.Y.; project administration, F.M., X.Q., Y.S., S.H. and L.Y.; funding acquisition, X.Q., Y.S., S.H. and L.Y. All authors have read and agreed to the published version of the manuscript.

Funding: This research was funded by the National Key R&D Program of China (Grant No. 2022YFD1400400).

Data Availability Statement: The original contributions presented in this study are included in the article, further inquiries can be directed to the corresponding author.

Acknowledgments: We sincerely thank the anonymous reviewers for their valuable suggestions, which have greatly enhanced the quality of this manuscript. We also acknowledge the Google Earth Engine platform for providing preprocessed Sentinel data.

Conflicts of Interest: The authors declare no conflicts of interest.

References

1. Ellison, D.; Morris, C.E.; Locatelli, B.; Sheil, D.; Cohen, J.; Murdiyarso, D.; Gutierrez, V.; Noordwijk, M.V.; Creed, I.F.; Pokorny, J.; et al. Trees, Forests and Water: Cool Insights for a Hot World. *Glob. Environ. Change* **2017**, *43*, 51–61. [CrossRef]
2. Seidl, R.; Thom, D.; Kautz, M. Forest disturbances under climate change. *Nat. Clim. Change* **2017**, *7*, 395–402. [CrossRef]
3. Teshome, D.T.; Zharare, G.E.; Naidoo, S. The Threat of the Combined Effect of Biotic and Abiotic Stress Factors in Forestry Under a Changing Climate. *Front. Plant Sci.* **2020**, *11*, 601009. [CrossRef]
4. Van Lierop, P.; Lindquist, E.; Sathyapala, S.; Franceschini, G. Global Forest Area Disturbance from Fire, Insect Pests, Diseases and Severe Weather Events. *For. Ecol. Manag.* **2015**, *352*, 78–88. [CrossRef]
5. Forzieri, G.; Girardello, M.; Ceccherini, G.; Spinoni, J.; Feyen, L.; Hartmann, H.; Beck, P.S.A.; Camps-Valls, G.; Chirici, G.; Mauri, A.; et al. Emergent Vulnerability to Climate-Driven Disturbances in European Forests. *Nat. Commun.* **2021**, *12*, 1081. [CrossRef] [PubMed]
6. Jactel, H.; Koricheva, J.; Castagneyrol, B. Responses of Forest Insect Pests to Climate Change: Not so Simple. *Curr. Opin. Insect Sci.* **2019**, *35*, 103–108. [CrossRef]
7. Lehmann, P.; Ammunét, T.; Barton, M.; Battisti, A.; Eigenbrode, S.D.; Jepsen, J.U.; Kalinkat, G.; Neuvonen, S.; Niemelä, P.; Terblanche, J.S.; et al. Complex Responses of Global Insect Pests to Climate Warming. *Front. Ecol. Environ.* **2020**, *18*, 141–150. [CrossRef]
8. Weed, A.; Ayres, M.; Hicke, J. Consequences of Climate Change for Biotic Disturbances in North American Forests. *Ecol. Monogr.* **2013**, *83*, 441–470. [CrossRef]
9. Zhang, S.; Shen, S.; Peng, J.; Zhou, X.; Kong, X.; Ren, P.; Liu, F.; Han, L.; Zhan, S.; Huang, Y.; et al. Chromosome-level Genome Assembly of an Important Pine Defoliator Dendrolimus Punctatus (Lepidoptera; Lasiocampidae). *Mol. Ecol. Resour.* **2020**, *20*, 1023–1037. [CrossRef] [PubMed]
10. Qin, J.; Zhang, Y.; Zhou, X.; Kong, X.; Wei, S.; Ward, R.D.; Zhang, A. Mitochondrial Phylogenomics and Genetic Relationships of Closely Related Pine Moth (Lasiocampidae: Dendrolimus) Species in China, Using Whole Mitochondrial Genomes. *BMC Genomics* **2015**, *16*, 428. [CrossRef]
11. Bao, Y.; Na, L.; Han, A.; Guna, A.; Wang, F.; Liu, X.; Zhang, J.; Wang, C.; Tong, S.; Bao, Y. Drought Drives the Pine Caterpillars (Dendrolimus Spp.) Outbreaks and Their Prediction under Different RCPs Scenarios: A Case Study of Shandong Province, China. *For. Ecol. Manag.* **2020**, *475*, 118446. [CrossRef]
12. Nansen, C.; Elliott, N. Remote Sensing and Reflectance Profiling in Entomology. *Annu. Rev. Entomol.* **2016**, *61*, 139–158. [CrossRef]
13. Berger, K.; Machwitz, M.; Kycko, M.; Kefauver, S.C.; Van Wittenberghe, S.; Gerhards, M.; Verrelst, J.; Atzberger, C.; van der Tol, C.; Damm, A.; et al. Multi-Sensor Spectral Synergies for Crop Stress Detection and Monitoring in the Optical Domain: A Review. *Remote Sens. Environ.* **2022**, *280*, 113198. [CrossRef]
14. Zhang, B.; Zhou, L.; Zhou, X.; Bai, Y.; Zhan, M.; Chen, J.; Xu, C. Differential Responses of Leaf Photosynthesis to Insect and Pathogen Outbreaks: A Global Synthesis. *Sci. Total Environ.* **2022**, *832*, 155052. [CrossRef]
15. Pineda, M.; Barón, M.; Pérez-Bueno, M.-L. Thermal Imaging for Plant Stress Detection and Phenotyping. *Remote Sens.* **2020**, *13*, 68. [CrossRef]
16. Lausch, A.; Heurich, M.; Gordalla, D.; Dobner, H.-J.; Gwillym-Margianto, S.; Salbach, C. Forecasting Potential Bark Beetle Outbreaks Based on Spruce Forest Vitality Using Hyperspectral Remote-Sensing Techniques at Different Scales. *For. Ecol. Manag.* **2013**, *308*, 76–89. [CrossRef]
17. Bhattarai, G.P.; Schmid, R.B.; McCornack, B.P. Remote Sensing Data to Detect Hessian Fly Infestation in Commercial Wheat Fields. *Sci. Rep.* **2019**, *9*, 6109. [CrossRef]
18. Hornero, A.; Zarco-Tejada, P.J.; Quero, J.L.; North, P.R.J.; Ruiz-Gómez, F.J.; Sánchez-Cuesta, R.; Hernandez-Clemente, R. Modelling Hyperspectral- and Thermal-Based Plant Traits for the Early Detection of Phytophthora-Induced Symptoms in Oak Decline. *Remote Sens. Environ.* **2021**, *263*, 112570. [CrossRef]
19. Gitelson, A.A.; Merzlyak, M.N. Remote Estimation of Chlorophyll Content in Higher Plant Leaves. *Int. J. Remote Sens.* **1997**, *18*, 2691–2697. [CrossRef]
20. Carter, G.A. RESPONSES OF LEAF SPECTRAL REFLECTANCE TO PLANT STRESS. *Am. J. Bot.* **1993**, *80*, 239–243. [CrossRef]
21. Ye, S.; Rogan, J.; Zhu, Z.; Eastman, J.R. A Near-Real-Time Approach for Monitoring Forest Disturbance Using Landsat Time Series: Stochastic Continuous Change Detection. *Remote Sens. Environ.* **2021**, *252*, 112167. [CrossRef]

22. Tang, X.; Bratley, K.H.; Cho, K.; Bullock, E.L.; Olofsson, P.; Woodcock, C.E. Near Real-Time Monitoring of Tropical Forest Disturbance by Fusion of Landsat, Sentinel-2, and Sentinel-1 Data. *Remote Sens. Environ.* **2023**, *294*, 113626. [CrossRef]
23. Abdullah, H.; Skidmore, A.K.; Darvishzadeh, R.; Heurich, M. Sentinel-2 Accurately Maps Green-Attack Stage of European Spruce Bark Beetle (Ips Typographus, L.) Compared with Landsat-8. *Remote Sens. Ecol. Conserv.* **2019**, *5*, 87–106. [CrossRef]
24. Huo, L.; Persson, H.J.; Lindberg, E. Early Detection of Forest Stress from European Spruce Bark Beetle Attack, and a New Vegetation Index: Normalized Distance Red & SWIR (NDRS). *Remote Sens. Environ.* **2021**, *255*, 112240. [CrossRef]
25. Candotti, A.; De Giglio, M.; Dubbini, M.; Tomelleri, E. A Sentinel-2 Based Multi-Temporal Monitoring Framework for Wind and Bark Beetle Detection and Damage Mapping. *Remote Sens.* **2022**, *14*, 6105. [CrossRef]
26. Reinosch, E.; Backa, J.; Adler, P.; Deutscher, J.; Eisnecker, P.; Hoffmann, K.; Langner, N.; Puhm, M.; Rüetschi, M.; Straub, C.; et al. Detailed Validation of Large-Scale Sentinel-2-Based Forest Disturbance Maps across Germany. *For. Int. J. For. Res.* **2025**, *98*, 437–453. [CrossRef]
27. Drusch, M.; Del Bello, U.; Carlier, S.; Colin, O.; Fernandez, V.; Gascon, F.; Hoersch, B.; Isola, C.; Laberinti, P.; Martimort, P.; et al. Sentinel-2: ESA's Optical High-Resolution Mission for GMES Operational Services. *Remote Sens. Environ.* **2012**, *120*, 25–36. [CrossRef]
28. Kumari, A.; Karthikeyan, S. Sentinel-2 Data for Land Use/Land Cover Mapping: A Meta-Analysis and Review. *SN Comput. Sci.* **2023**, *4*, 815. [CrossRef]
29. Clevers, J.G.P.W.; Gitelson, A.A. Remote Estimation of Crop and Grass Chlorophyll and Nitrogen Content Using Red-Edge Bands on Sentinel-2 and -3. *Int. J. Appl. Earth Obs. Geoinf.* **2013**, *23*, 344–351. [CrossRef]
30. Zarco-Tejada, P.J.; Hornero, A.; Beck, P.S.A.; Kattenborn, T.; Kempeneers, P.; Hernández-Clemente, R. Chlorophyll Content Estimation in an Open-Canopy Conifer Forest with Sentinel-2A and Hyperspectral Imagery in the Context of Forest Decline. *Remote Sens. Environ.* **2019**, *223*, 320–335. [CrossRef] [PubMed]
31. Zhang, J.; Cong, S.; Zhang, G.; Ma, Y.; Zhang, Y.; Huang, J. Detecting Pest-Infested Forest Damage through Multispectral Satellite Imagery and Improved UNet++. *Sensors* **2022**, *22*, 7440. [CrossRef] [PubMed]
32. Pasquarella, V.J.; Holden, C.E.; Woodcock, C.E. Improved Mapping of Forest Type Using Spectral-Temporal Landsat Features. *Remote Sens. Environ.* **2018**, *210*, 193–207. [CrossRef]
33. Meigs, G.; Kennedy, R.; Cohen, W. A Landsat Time Series Approach to Characterize Bark Beetle and Defoliator Impacts on Tree Mortality and Surface Fuels in Conifer Forests. *Remote Sens. Environ.* **2011**, *115*, 3707–3718. [CrossRef]
34. Bright, B.C.; Hudak, A.T.; Kennedy, R.E.; Braaten, J.D.; Henareh Khalyani, A. Examining Post-Fire Vegetation Recovery with Landsat Time Series Analysis in Three Western North American Forest Types. *Fire Ecol.* **2019**, *15*, 8. [CrossRef]
35. Verbesselt, J.; Hyndman, R.; Newnham, G.; Culvenor, D. Detecting Trend and Seasonal Changes in Satellite Image Time Series. *Remote Sens. Environ.* **2010**, *114*, 106–115. [CrossRef]
36. Zhu, Z.; Woodcock, C.E. Continuous Change Detection and Classification of Land Cover Using All Available Landsat Data. *Remote Sens. Environ.* **2014**, *144*, 152–171. [CrossRef]
37. Cohen, W.B.; Yang, Z.; Healey, S.P.; Kennedy, R.E.; Gorelick, N. A LandTrendr Multispectral Ensemble for Forest Disturbance Detection. *Remote Sens. Environ.* **2018**, *205*, 131–140. [CrossRef]
38. Brooks, E.B.; Wynne, R.H.; Thomas, V.A. Using Window Regression to Gap-Fill Landsat ETM+ Post SLC-Off Data. *Remote Sens.* **2018**, *10*, 1502. [CrossRef]
39. Meddens, A.J.H.; Hicke, J.A.; Vierling, L.A.; Hudak, A.T. Evaluating Methods to Detect Bark Beetle-Caused Tree Mortality Using Single-Date and Multi-Date Landsat Imagery. *Remote Sens. Environ.* **2013**, *132*, 49–58. [CrossRef]
40. Rahimzadeh-Bajgiran, P.; Weiskittel, A.R.; Kneeshaw, D.; MacLean, D.A. Detection of Annual Spruce Budworm Defoliation and Severity Classification Using Landsat Imagery. *Forests* **2018**, *9*, 357. [CrossRef]
41. Jamali, S.; Olsson, P.-O.; Ghorbanian, A.; Müller, M. Examining the Potential for Early Detection of Spruce Bark Beetle Attacks Using Multi-Temporal Sentinel-2 and Harvester Data. *ISPRS J. Photogramm. Remote Sens.* **2023**, *205*, 352–366. [CrossRef]
42. Maxwell, A.E.; Warner, T.A.; Fang, F. Implementation of Machine-Learning Classification in Remote Sensing: An Applied Review. *Int. J. Remote Sens.* **2018**, *39*, 2784–2817. [CrossRef]
43. Bhattarai, R.; Rahimzadeh-Bajgiran, P. Optimizing Forest Defoliation Detection Using Remote Sensing Data: A Multi–Resolution Approach Using Machine Learning Algorithms. *Trees For. People* **2025**, *22*, 101009. [CrossRef]
44. Breiman, L. Random Forests. *Mach. Learn.* **2001**, *45*, 5–32. [CrossRef]
45. Belgiu, M.; Drăguţ, L. Random Forest in Remote Sensing: A Review of Applications and Future Directions. *ISPRS J. Photogramm. Remote Sens.* **2016**, *114*, 24–31. [CrossRef]
46. Pelletier, C.; Valero, S.; Inglada, J.; Champion, N.; Dedieu, G. Assessing the Robustness of Random Forests to Map Land Cover with High Resolution Satellite Image Time Series over Large Areas. *Remote Sens. Environ.* **2016**, *187*, 156–168. [CrossRef]
47. Talukdar, S.; Singha, P.; Mahato, S.; Shahfahad; Pal, S.; Liou, Y.-A.; Rahman, A. Land-Use Land-Cover Classification by Machine Learning Classifiers for Satellite Observations—A Review. *Remote Sens.* **2020**, *12*, 1135. [CrossRef]

48. Mountrakis, G.; Im, J.; Ogole, C. Support Vector Machines in Remote Sensing: A Review. *ISPRS J. Photogramm. Remote Sens.* **2011**, *66*, 247. [CrossRef]
49. Pal, M.; Mather, P.M. Support Vector Machines for Classification in Remote Sensing. *Int. J. Remote Sens.* **2005**, *26*, 1007–1011. [CrossRef]
50. Zhang, C.; Sargent, I.; Pan, X.; Li, H.; Gardiner, A.; Hare, J.; Atkinson, P.M. Joint Deep Learning for Land Cover and Land Use Classification. *Remote Sens. Environ.* **2019**, *221*, 173–187. [CrossRef]
51. Yuan, Q.; Shen, H.; Li, T.; Li, Z.; Li, S.; Jiang, Y.; Xu, H.; Tan, W.; Yang, Q.; Wang, J.; et al. Deep Learning in Environmental Remote Sensing: Achievements and Challenges. *Remote Sens. Environ.* **2020**, *241*, 111716. [CrossRef]
52. Rußwurm, M.; Körner, M. Self-Attention for Raw Optical Satellite Time Series Classification. *ISPRS J. Photogramm. Remote Sens.* **2020**, *169*, 421–435. [CrossRef]
53. Ball, J.E.; Anderson, D.T.; Chan, C.S. Comprehensive Survey of Deep Learning in Remote Sensing: Theories, Tools, and Challenges for the Community. *J. Appl. Remote Sens.* **2017**, *11*, 1. [CrossRef]
54. Zhao, Y.; Luo, Y. Wavelet Analysis on Temperature and Precipitation Changes in Dabie Mountain of West Anhui. *J. Phys. Conf. Ser.* **2021**, *1732*, 012105. [CrossRef]
55. Zhou, G.; Peng, C.; Li, Y.; Liu, S.; Zhang, Q.; Tang, X.; Liu, J.; Yan, J.; Zhang, D.; Chu, G. A Climate Change-Induced Threat to the Ecological Resilience of a Subtropical Monsoon Evergreen Broad-Leaved Forest in Southern China. *Glob. Change Biol.* **2013**, *19*, 1197–1210. [CrossRef]
56. Busing, R.; White, R.; Harmon, M.; White, P. Hurricane Disturbance in a Temperate Deciduous Forest: Patch Dynamics, Tree Mortality, and Coarse Woody Detritus. *Plant Ecol.* **2009**, *201*, 351–363. [CrossRef]
57. Jactel, H.; Petit, J.; Desprez-Loustau, M.; Delzon, S.; Piou, D.; Battisti, A.; Koricheva, J. Drought Effects on Damage by Forest Insects and Pathogens: A Meta-Analysis. *Glob. Change Biol.* **2012**, *18*, 267–276. [CrossRef]
58. Wang, Q.; Shi, W.; Li, Z.; Atkinson, P.M. Fusion of Sentinel-2 Images. *Remote Sens. Environ.* **2016**, *187*, 241–252. [CrossRef]
59. Gascon, F.; Bouzinac, C.; Thépaut, O.; Jung, M.; Francesconi, B.; Louis, J.; Lonjou, V.; Lafrance, B.; Massera, S.; Gaudel-Vacaresse, A.; et al. Copernicus Sentinel-2A Calibration and Products Validation Status. *Remote Sens.* **2017**, *9*, 584. [CrossRef]
60. Bragard, C.; Baptista, P.; Chatzivassiliou, E.; Di Serio, F.; Gonthier, P.; Jaques Miret, J.A.; Justesen, A.F.; Magnusson, C.S.; Milonas, P.; Navas-Cortes, J.A.; et al. Pest Categorisation of Dendrolimus Punctatus. *EFSA J.* **2024**, *22*, e8504. [CrossRef]
61. Li, D.; Tong, Q.; Li, R.; Gong, J.; Zhang, L. Current Issues in High-Resolution Earth Observation Technology. *Sci. China Earth Sci.* **2012**, *55*, 1043–1051. [CrossRef]
62. Vivone, G.; Alparone, L.; Chanussot, J.; Dalla Mura, M.; Garzelli, A.; Licciardi, G.A.; Restaino, R.; Wald, L. A Critical Comparison Among Pansharpening Algorithms. *IEEE Trans. Geosci. Remote Sens.* **2015**, *53*, 2565–2586. [CrossRef]
63. Liu, L.; Zhang, X.; Gao, Y.; Chen, X.; Shuai, X.; Mi, J. Finer-Resolution Mapping of Global Land Cover: Recent Developments, Consistency Analysis, and Prospects. *J. Remote Sens.* **2021**, *2021*, 2021/5289697. [CrossRef]
64. Griffiths, P.; van der Linden, S.; Kuemmerle, T.; Hostert, P. A Pixel-Based Landsat Compositing Algorithm for Large Area Land Cover Mapping. *IEEE J. Sel. Top. Appl. Earth Obs. Remote Sens.* **2012**, *6*, 2088–2101. [CrossRef]
65. Näsi, R.; Honkavaara, E.; Lyytikäinen-Saarenmaa, P.; Blomqvist, M.; Litkey, P.; Hakala, T.; Viljanen, N.; Kantola, T.; Tanhuanpää, T.; Holopainen, M. Using UAV-Based Photogrammetry and Hyperspectral Imaging for Mapping Bark Beetle Damage at Tree-Level. *Remote Sens.* **2015**, *7*, 15467–15493. [CrossRef]
66. Murfitt, J.; He, Y.; Yang, J.; Mui, A.; De Mille, K. Ash Decline Assessment in Emerald Ash Borer Infested Natural Forests Using High Spatial Resolution Images. *Remote Sens.* **2016**, *8*, 256. [CrossRef]
67. Wilson, E.H.; Sader, S.A. Detection of Forest Harvest Type Using Multiple Dates of Landsat TM Imagery. *Remote Sens. Environ.* **2002**, *80*, 385–396. [CrossRef]
68. Frampton, W.J.; Dash, J.; Watmough, G.; Milton, E.J. Evaluating the Capabilities of Sentinel-2 for Quantitative Estimation of Biophysical Variables in Vegetation. *ISPRS J. Photogramm. Remote Sens.* **2013**, *82*, 83–92. [CrossRef]
69. Huete, A.R. A Soil-Adjusted Vegetation Index (SAVI). *Remote Sens. Environ.* **1988**, *25*, 295–309. [CrossRef]
70. Tucker, C.J. Red and Photographic Infrared Linear Combinations for Monitoring Vegetation. *Remote Sens. Environ.* **1979**, *8*, 127–150. [CrossRef]
71. Huete, A.; Didan, K.; Miura, T.; Rodriguez, E.P.; Gao, X.; Ferreira, L.G. Overview of the Radiometric and Biophysical Performance of the MODIS Vegetation Indices. *Remote Sens. Environ.* **2002**, *83*, 195–213. [CrossRef]
72. Escuin, S.; Navarro, R.; Fernández, P. Fire Severity Assessment by Using NBR (Normalized Burn Ratio) and NDVI (Normalized Difference Vegetation Index) Derived from LANDSAT TM/ETM Images. *Int. J. Remote Sens.* **2008**, *29*, 1053–1073. [CrossRef]
73. Kantola, T.; Vastaranta, M.; Yu, X.; Lyytikainen-Saarenmaa, P.; Holopainen, M.; Talvitie, M.; Kaasalainen, S.; Solberg, S.; Hyyppa, J. Classification of Defoliated Trees Using Tree-Level Airborne Laser Scanning Data Combined with Aerial Images. *Remote Sens.* **2010**, *2*, 2665–2679. [CrossRef]
74. Atzberger, C. Advances in Remote Sensing of Agriculture: Context Description, Existing Operational Monitoring Systems and Major Information Needs. *Remote Sens.* **2013**, *5*, 949–981. [CrossRef]

75. Sheykhmousa, M.; Mahdianpari, M.; Ghanbari, H.; Mohammadimanesh, F.; Ghamisi, P.; Homayouni, S. Support Vector Machine Versus Random Forest for Remote Sensing Image Classification: A Meta-Analysis and Systematic Review. *IEEE J. Sel. Top. Appl. Earth Obs. Remote Sens.* **2020**, *13*, 6308–6325. [CrossRef]
76. Stehman, S.V.; Foody, G.M. Key Issues in Rigorous Accuracy Assessment of Land Cover Products. *Remote Sens. Environ.* **2019**, *231*, 111199. [CrossRef]
77. Illarionova, S.; Tregubova, P.; Shukhratov, I.; Shadrin, D.; Kedrov, A.; Burnaev, E. Remote Sensing Data Fusion Approach for Estimating Forest Degradation: A Case Study of Boreal Forests Damaged by Polygraphus Proximus. *Front. Environ. Sci.* **2024**, *12*, 1412870. [CrossRef]
78. Wulder, M.A.; White, J.C.; Bentz, B.; Alvarez, M.F.; Coops, N.C. Estimating the Probability of Mountain Pine Beetle Red-Attack Damage. *Remote Sens. Environ.* **2006**, *101*, 150–166. [CrossRef]
79. Liu, L.; Coops, N.C.; Aven, N.W.; Pang, Y. Mapping Urban Tree Species Using Integrated Airborne Hyperspectral and LiDAR Remote Sensing Data. *Remote Sens. Environ.* **2017**, *200*, 170–182. [CrossRef]
80. XU, Z.; LIU, J.; YU, K.; GONG, C.; XIE, W.; TANG, M.; LAI, R.; LI, Z. Spectral Features Analysis of Pinus Massoniana with Pest of Dendrolimus Punctatus Walker and Levels Detection. *Spectrosc. Spectr. Anal.* **2013**, *33*, 428–433. [CrossRef]
81. Hais, M.; Jonášová, M.; Langhammer, J.; Kučera, T. Comparison of Two Types of Forest Disturbance Using Multitemporal Landsat TM/ETM+ Imagery and Field Vegetation Data. *Remote Sens. Environ.* **2009**, *113*, 835–845. [CrossRef]
82. He-Ya, S.; Huang, X.; Zhou, D.; Zhang, J.; Bao, G.; Tong, S.; Bao, Y.; Ganbat, D.; Tsagaantsooj, N.; Altanchimeg, D.; et al. Identification of Larch Caterpillar Infestation Severity Based on Unmanned Aerial Vehicle Multispectral and LiDAR Features. *Forests* **2024**, *15*, 191. [CrossRef]
83. Guo, J.; Huang, X.; Zhou, D.; Zhang, J.; Bao, G.; Tong, S.; Bao, Y.; Ganbat, D.; Altanchimeg, D.; Enkhnasan, D.; et al. Estimation of the Water Content of Needles under Stress by Erannis Jacobsoni Djak. via Sentinel-2 Satellite Remote Sensing. *Front. Plant Sci.* **2025**, *16*, 1540604. [CrossRef]
84. Spruce, J.P.; Sader, S.; Ryan, R.E.; Smoot, J.; Kuper, P.; Ross, K.; Prados, D.; Russell, J.; Gasser, G.; McKellip, R.; et al. Assessment of MODIS NDVI Time Series Data Products for Detecting Forest Defoliation by Gypsy Moth Outbreaks. *Remote Sens. Environ.* **2011**, *115*, 427–437. [CrossRef]
85. Fassnacht, F.E.; Latifi, H.; Stereńczak, K.; Modzelewska, A.; Lefsky, M.; Waser, L.T.; Straub, C.; Ghosh, A. Review of Studies on Tree Species Classification from Remotely Sensed Data. *Remote Sens. Environ.* **2016**, *186*, 64–87. [CrossRef]
86. Hermosilla, T.; Wulder, M.A.; White, J.C.; Coops, N.C.; Hobart, G.W.; Campbell, L.B. Mass Data Processing of Time Series Landsat Imagery: Pixels to Data Products for Forest Monitoring. *Int. J. Digit. Earth* **2016**, *9*, 1035–1054. [CrossRef]

Disclaimer/Publisher's Note: The statements, opinions and data contained in all publications are solely those of the individual author(s) and contributor(s) and not of MDPI and/or the editor(s). MDPI and/or the editor(s) disclaim responsibility for any injury to people or property resulting from any ideas, methods, instructions or products referred to in the content.